ADVANCED HEALTHCARE MATERIALS
www.advhealthmat.de

Nanocatalytic Therapy for Pneumonia by a Hetero-Element-Doped Carbon Nanozyme

*Min Zhou, Minxuan Zhang, Jiayuan Feng, Fuying Zhu, Tong Li, Qi Mei, Gen Wei, and Hui Wei**

Pneumonia continues to be complicated by its progression to acute lung injury (ALI). The onset of ALI is linked to an overproduction of reactive oxygen species (ROS) and a severe inflammatory response. Therefore, the rapid mitigation of ROS and inflammation is crucial in addressing ALI. Concurrently, prompt bacterial elimination is necessary for bacteria-induced ALI. Here, a Co-based carbon nanozyme (CN) with enhanced enzyme-like activities is developed by co-doping with a small amount of Mn (CoMn CN). Compared to cobalt CN without Mn co-doping (Co CN), the active sites of Co and its coordination with N in CoMn CN are slightly altered, resulting in enhanced oxidase (OXD)-, peroxidase (POD)-, superoxide dismutase (SOD)-, and catalase (CAT)-like activities. Given the enhanced enzyme-like activities, its applications for lipopolysaccharide (LPS)- and methicillin-resistant *Staphylococcus aureus* (MRSA)-induced ALI treatments are explored. CoMn CN demonstrates superior efficacy in both LPS- and MRSA-induced ALI models, effectively combining rapid scavenging of ROS and inflammation with subsequently bacterial elimination. Consequently, a novel type of Co-based CN by Mn co-doping is developed to augment enzyme-like activities, offering significant protective effects against ALI. This study not only broadens the application of Co-based CNs but also shows a promising strategy for ALI therapy.

1. Introduction

Pneumonia, particularly infectious pneumonia, continues to pose a significant challenge due to its potential to induce acute lung injury (ALI) and acute respiratory distress, leading to pulmonary edema, hypoxemia, respiratory failure, and even mortality.[1,2] Pathogenesis investigations have identified that virus and bacteria as the predominant causative agents in definitive ALI. Notably, bacterial infections often arise as secondary complications of viral infections, further intensifying the severity of ALI.[3–5] Regardless of the specific type of ALI, rapid and effective therapeutic interventions are urgently needed to prevent respiratory failure. Clinical manifestations of ALI are typically linked to an overproduction of reactive oxygen species (ROS) and a pronounced inflammatory response. Consequently, current therapeutics for ALI predominantly focus on anti-oxidants (e.g., curcumin, naringenin, and nicotinamide adenine dinucleotide phosphate (NADPH) oxidase inhibitors) to scavenge ROS, glucocorticoids (e.g., dexamethasone) to mitigate inflammatory cytokines, and antibiotics to address bacterial infections.[6–10] Nevertheless, these strategies frequently encounter limitations due to their inability to simultaneously scavenge ROS, mitigate inflammation, and combat bacterial infections, resulting in higher dosage, prolonged treatment durations, and even drug resistance.[11] Therefore, the development of therapeutic strategies that integrating ROS scavenging, inflammation alleviation, and antibacterial capabilities together is essential for more effective treatment of ALI. Despite significant

M. Zhou, M. Zhang, J. Feng, F. Zhu, T. Li, Q. Mei, G. Wei, H. Wei
Department of Biomedical Engineering
College of Engineering and Applied Sciences
Nanjing National Laboratory of Microstructures
Jiangsu Key Laboratory of Artificial Functional Materials
Nanjing University
Nanjing, Jiangsu 210023, China
E-mail: weihui@nju.edu.cn

H. Wei
Nanozyme Laboratory in Zhongyuan
Henan Academy of Innovations in Medical Science
Zhengzhou, Henan 451163, China

H. Wei
State Key Laboratory of Analytical Chemistry for Life Science
School of Chemistry and Chemical Engineering
Chemistry and Biomedicine Innovation Center (ChemBIC)
ChemBioMed Interdisciplinary Research Centre at Nanjing University
Nanjing University
Nanjing, Jiangsu 210023, China

F. Zhu
Medical School of Nanjing University
Nanjing, Jiangsu 210023, China

G. Wei
Medical College
Institute of Translational Medicine
Yangzhou University
Yangzhou, Jiangsu 225009, China

The ORCID identification number(s) for the author(s) of this article can be found under https://doi.org/10.1002/adhm.202500725

DOI: 10.1002/adhm.202500725

advancements in nanomedicine, combinatory therapies for ALI remains challenging. To address this gap, we develop a multifunctional nanozyme-enabled therapy for ALI.

Nanozymes, the functional nanomaterials possessing enzyme-like activities, have been applied to treat diseases such as inflammatory bowel disease, acute kidney injury, and bacterial infections.[12–19] Recently, many nanozymes have been developed for ALI therapy, effectively protecting the lungs by utilizing superoxide dismutase (SOD)- or catalase (CAT)-like activities.[20–23] However, these treatments often neglect the anti-microbial aspect, which is crucial for comprehensive ALI therapy. Thus, developing multifunctional nanozymes with anti-oxidant, anti-inflammatory, and anti-microbial properties is a promising approach for ALI therapy.

Among the developed therapeutic nanozymes, Co-based nanozymes have gained prominence in recent years due to their regulatable oxidation state, including Co (II) and Co (III). These oxidation states confer remarkable enzymatic activities to Co-based nanozymes.[24] The enzymatic performance is primarily influenced by the Co-based active species, such as Co-N, Co-O, and Co-Co, which can be precisely modulated to achieve desired enzyme-like activities for applications in biosensing and biomedicine.[24–29] Notably, hetero-elements incorporation for Co-based CNs has been shown to significantly enhance their enzyme-like activities. For instance, iron (Fe) co-doping has been applied to develop specific peroxidase (POD)-like Co-based nanozymes for sensing applications, and copper (Cu) co-doping has been employed to produce CuCo nanozymes exhibiting high POD- and oxidase (OXD)-like activities for anti-microbial purposes.[30–32]

Although Co-based nanozymes have achieved notable progress in diverse fields, their application in ALI therapy remains constrained. Notably, manganese (Mn)-based nanozymes have been investigated for the treatment of inflammatory diseases, attributing to their anti-inflammatory properties.[33–35] However, there has been limited research on modulating the active species of cobalt through Mn co-doping for ALI treatment. In this study, we propose a Mn co-doping Co-based nanozyme for ALI therapy. Zeolitic imidazolate framework-8 (ZIF-8) was chosen as a pyrolysis template for the synthesis of doped carbon nanozymes (CNs), specifically Co CN, CoMn CN, and Mn CN. Among these, CoMn CN exhibited the highest enzyme-like activities, including SOD, CAT, POD, and OXD. This enhancement is primarily attributed to alterations in Co's oxidation state and coordination environment. Given the enhanced enzyme-like activities of CoMn CN, we investigated its efficacy both in lipopolysaccharide (LPS)- and methicillin-resistant *Staphylococcus aureus* (MRSA)-induced ALI models. The results demonstrated effective ALI protection through simultaneous ROS scavenging, inflammation alleviation, and antibacterial ability.

2. Results and Discussion

2.1. Synthesis and Characterization of Co-Based CNs

CoMn CN was prepared by using ZIF-8 as a pyrolysis template (**Figure 1a**). First, CoMn@ZIF-8 precursors were synthesized according to a one-pot hydrothermal method with some modification.[36] Single metal-doped Co/Mn CNs (i.e., Co CN and Mn CN) were synthesized for comparison. Typically, Co^{2+} and/or Mn^{2+} were mixed with Zn^{2+} and 2-methylimidazole for precursors' synthesis (e.g., Co@ZIF-8, CoMn@ZIF-8, and Mn@ZIF-8). The detailed precursor compositions were listed in Table S1 (Supporting Information). These precursors were imaged using scanning electron microscope (SEM), and all demonstrated a similar dodecahedral morphology (Figure S1, Supporting Information). Then, the precursors were pyrolyzed at 950 °C under N_2 condition to obtain Co/Mn CNs. The obtained CNs demonstrated a similar morphology with the precursors, as observed by transmission electron microscopy (TEM) imaging (Figure S2, Supporting Information). Dynamic light scattering (DLS) analysis demonstrated the differences in the average hydrodynamic diameter (Figure S3, Supporting Information) and zeta potential (Figure S4, Supporting Information) for these CNs, with Mn CN exhibiting the largest hydrodynamic diameter and highest positive charge, likely due to the Mn doping.

To identify the CNs' crystalline structure, X-ray diffraction (XRD) was performed (Figure 1b). All nanozymes showed a broad peak from 20 to 30 degree, which was attributed to the (002) plane of the graphitic carbon. Two sharp peaks presented at 44.2 degree and 51.5 degree, matching well with the planes (100) and (101) of the metallic cobalt (PDF#15-0806).[37] Since there was no obvious changes in XRD patterns after Mn co-doping in CoMn CN, high-resolution TEM (HRTEM) imaging was performed to study the detailed structure of CoMn CN. As shown in Figure 1c, an interplanar distance of 0.205 nm was observed, representing the (111) plane of metallic Co,[38,39] which confirmed the presence of metallic Co in CoMn CN. Since CoMn CN and Co CN exhibited the similar morphology and crystalline structure, the Co and Mn content in each nanozyme were measured using inductively coupled plasma-optical emission spectrometry (ICP-OES) (Figure S5, Supporting Information). We found that Mn doping ratio was 0.18 wt% (weight percentage) for Mn CN and 0.16 wt% for CoMn CN, respectively. Previous reports demonstrated that Mn ions could not easily coordinate with ZIF-8 precursors, leading to low Mn content in one-step doping methods,[40] so the low Mn doping in our strategy was reasonable. Meanwhile, we performed element analysis for these CNs. The results showed that Mn consituted only a small portion in both Mn CN and CoMn CN (Table S2, Supporting Information). This low Mn doping could finely regulate the Co's active sites without significantly altering the overall composition. Meanwhile, no detectable Zn content remained in these CNs due to its relatively low boiling point (Zn boiling point: 906 °C).[41]

Next, the enzyme-like activities of these nanozymes were evaluated. First, the OXD-like activity was tested using 3,3′,5,5′-tetramethylbenzidine (TMB) as a reducing substrate in a pH 4.5 acetate buffer. CoMn CN exhibited the highest OXD-like activity, with a 1.25-fold enhancement than Co CN, while no obvious OXD-like activity of Mn CN was shown (Figure 1d). The OXD-like activity was in a concentration- and pH-dependent manner, with the best performance observed at pH 4.5 (Figure 1e; Figure S6, Supporting Information). The POD-like activity was investigated using the oxygen-insensitive terephthalic acid (TA) as the substrate, minimizing the interference from the OXD-like activity. Similarly, CoMn CN showed the highest POD-like activity in a pH- and concentration-dependent manner (Figure 1f,g;

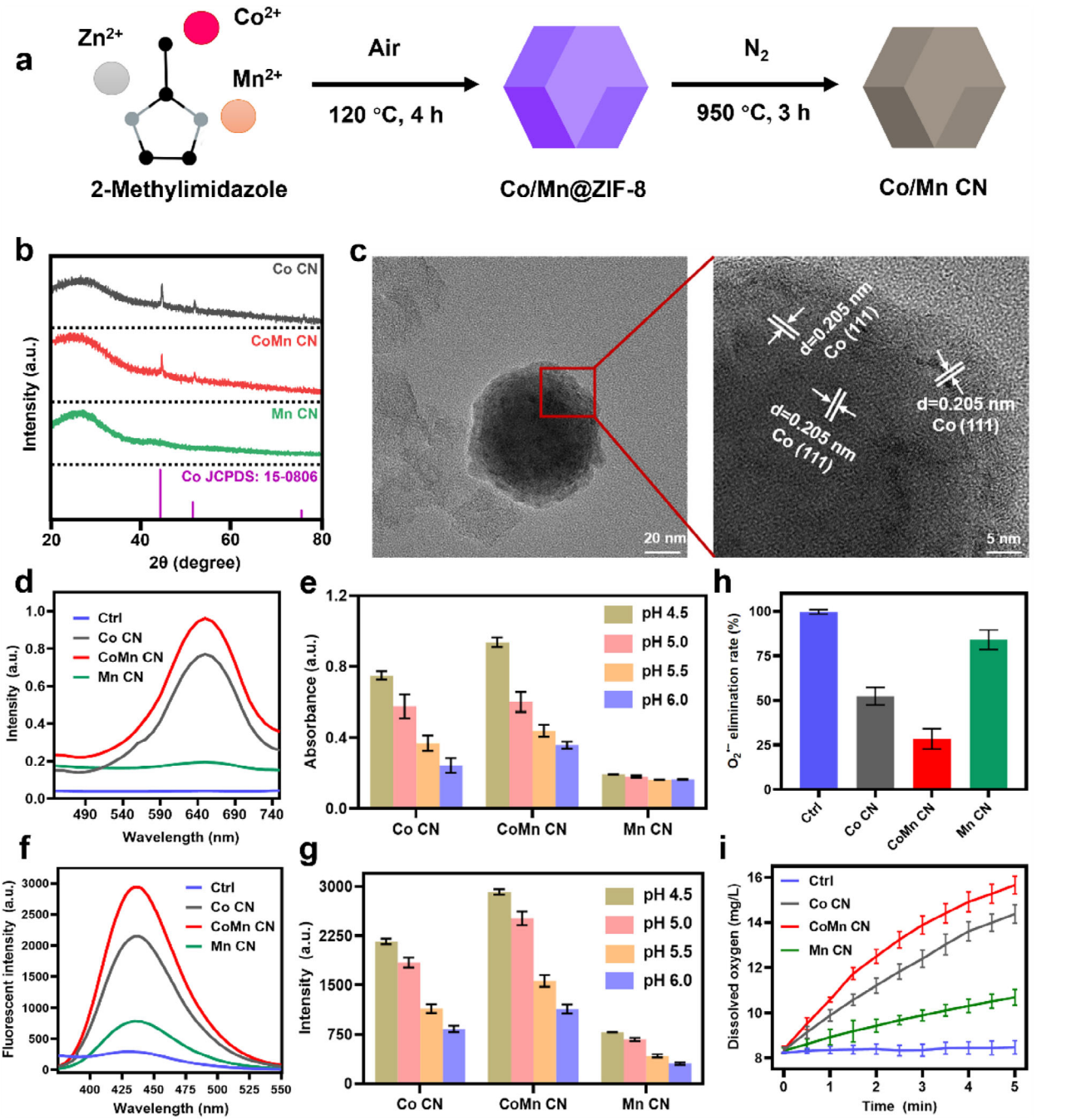

Figure 1. Characterization of Co-based CNs. a) Scheme of Co-based CNs' synthesis. b) XRD patterns of synthesized CNs. c) HRTEM images of CoMn CN. Interplanar distance represents the (111) plane of metallic Co. d) Measurement of OXD-like activities using absorption spectra. TMB (3,3′,5,5′-tetramethylbenzidine) as the substrate, incubating 10 μg mL^{-1} each CN in a pH 4.5 buffer. e) Measurement of OXD-like activities in different pH buffers with a microplate reader. f) Measurement of POD-like activities with a fluorescence spectrometer. TA (terephthalic acid) as the substrate, incubating 10 μg mL^{-1} each CN in a pH 4.5 buffer. g) Measurement of POD-like activities in different pH buffers with a microplate reader. h) Measurement of SOD-like activities by measuring $O_2^{\bullet-}$ scavenging. i) Measurement of CAT-like activities by measuring oxygen generation. Data (in e, g, h, and i) represent mean ± standard deviation (n = 4).

Figure S7, Supporting Information). Furthermore, the SOD- and CAT-like activities were evaluated by measuring superoxide anions ($O_2^{\bullet-}$) scavenging and oxygen generation in a pH 7.4 phosphate buffer (Figure 1h,i), respectively. CoMn CN also exhibited the highest $O_2^{\bullet-}$ scavenging and oxygen generation efficiency, following the same trend as the OXD- and POD-like activities. Compared with Co CN, CoMn CN exhibited better performance on four types of enzyme-like activities. However, no significant differences were observed in their XRD patterns, indicating the need for further mechanistic exploration.

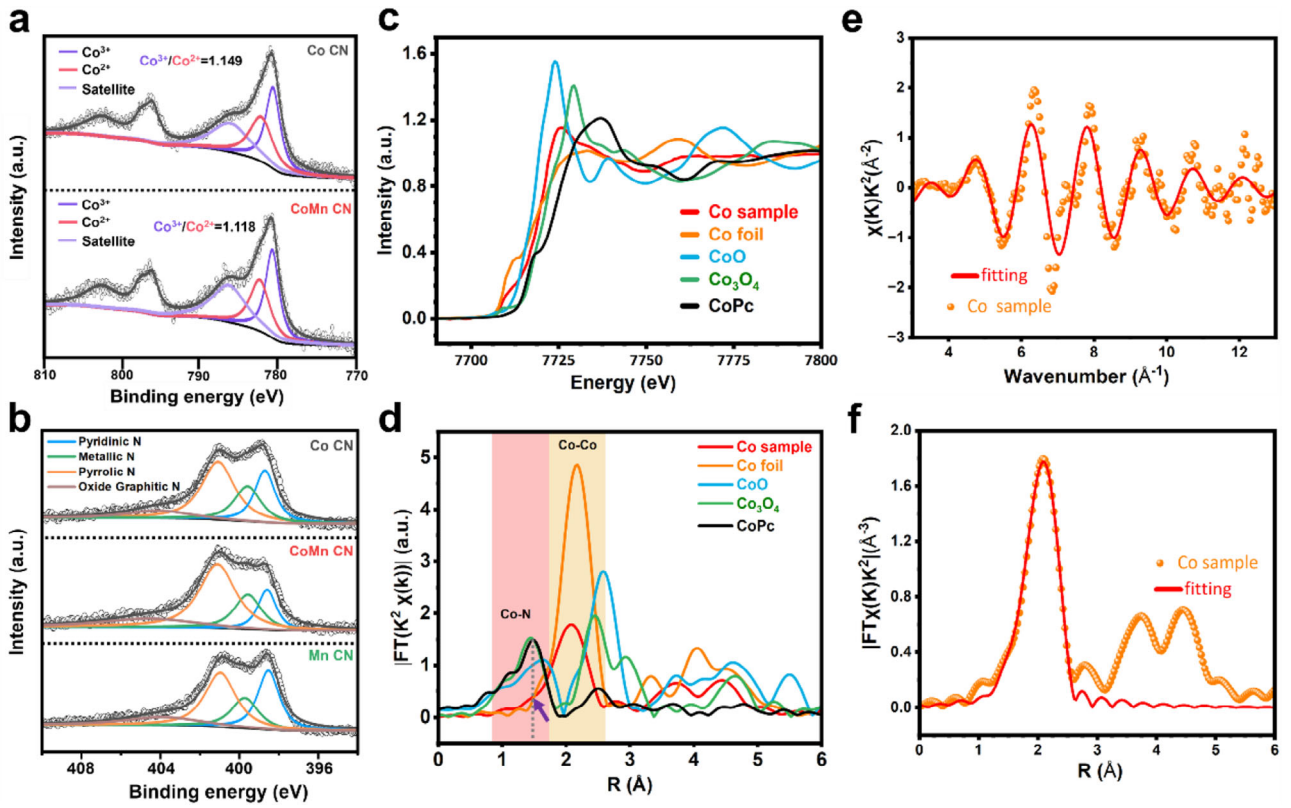

Figure 2. a) High-resolution XPS spectra of Co 2*p* in Co CN and CoMn CN. Sat. represents satellite. b) High-resolution XPS spectra of N 1*s*. c) XANES and d) EXAFS spectra of CoMn CN, references as Co foil, CoPc, CoO, and Co_3O_4. e) EXAFS spectrum (points) and fit curve (line) for CoMn CN, shown in R-edge (FT magnitude and imaginary component). f) EXAFS spectrum (points) and fit curve (line) for CoMn CN, shown in K-edge.

2.2. Exploration of CoMn CNs' Active Sites

To understand the mechanism of the enhanced enzyme-like activities for CoMn CN after Mn co-doping, we first explored the effect of Mn co-doping on the oxidation state of Co. X-ray photoelectron spectroscopy (XPS) was performed to identify the oxidation state of Co. The XPS survey spectra exhibited characteristic binding energies near 280 eV for C 1*s*, 400 eV for N 1*s*, and 800 eV for Co 2*p* (Figure S8, Supporting Information). There was no obvious peak for Mn, mainly due to its low content, which was consistent with the ICP-OES measurement (Figure S5, Supporting Information). Then, the high-resolution XPS spectra of Co 2*p* in Co CN and CoMn CN were analyzed (**Figure 2a**). The binding energy of Co 2*p* in CoMn CN was lower than that in Co CN, and the ratio of Co^{3+}/Co^{2+} decreased from 1.149 (in Co CN) to 1.118 (in CoMn CN). These changes were responsible for the enhancement in OXD- and POD-like activities of CoMn CN. Furthermore, X-ray absorption fine structure (XAFS) measurement was performed for CoMn CN characterization. The K-edge X-ray absorption near-edge structure (XANES) spectrum of CoMn CN was located between that of Co foil, CoO, Co_3O_4, and cobalt phthalocyanine (CoPc) (Figure 2c), suggesting the valence states of Co species as Co (0), Co (II), and Co (III). While the Co (0) can be contributed to the metallic cobalt, the coordination of Co (II) and Co (III) remained unclear.

To explore the coordination of Co (II) and Co (III), we examined the high-resolution XPS spectra of N 1*s*, which exhibited four distinct peaks belonging to oxide graphitic N, pyridinic N, pyrrolic N, and metallic N, respectively. Based on the Mn co-doping, N coordinating environment in CoMn CN was obviously changed (Figure 2b). Based on the changing of N coordination in CoMn CN, the extended X-ray absorption fine structure (EXAFS) spectrum was performed for further CoMn CN analysis (Figure 2d). CoMn CN demonstrated a prominent peak of Co foil, which was consistent with XRD pattern (Figure 1b). Furthermore, a weak peak emerged at 1.5 Å, which was close to CoPc peak. Coincidently, EXAFS curve fitting both at the Co R-edge and K-edge (Figure 2e,f) demonstrated the Co—N and Co—Co coordination. The Co-N coordination number and Co-Co coordination number in CoMn CN were 2.3±0.3 and 4.8±0.4, respectively (Table S3, Supporting Information). From these results, we regarded that Co has the coordination with N in our CoMn CN, and this was also consistent with the existing of Co (II) and Co (III). Consequently, we speculated that the metallic Co and Co-N_x were the main compositions for CoMn CN. Based on Mn co-doping, valence state of Co and N coordinating environment were changed, thus exhibiting the enhancement for enzyme-like activities in CoMn CN.

2.3. Anti-Microbial Capacity of Co-Based CNs

Based on above analysis of CNs' OXD- and POD-like activities, we investigated their anti-microbial potential. First, MRSA

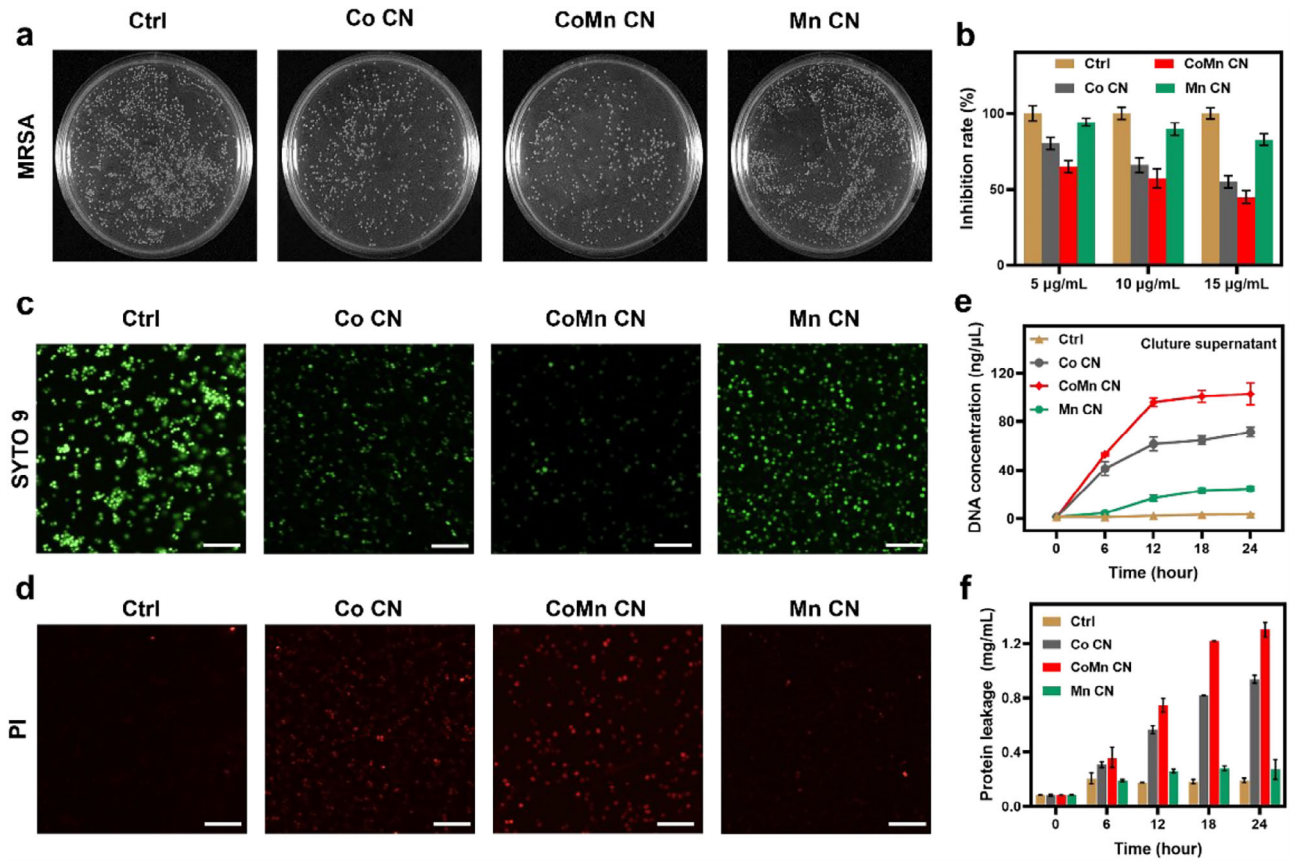

Figure 3. Anti-microbial capacity of Co-based CNs. a) Digital photos of MRSA clone formation by indicated treatments. Concentration of nanozymes sets as 10 μg mL^{-1}. b) Concentration dependent growth inhibition by nanozymes mediated. Fluorescent images of c) live and d) dead MRSA. Green fluorescence represents SYTO 9 and red fluorescence represents PI (Propidium Iodide). (SYTO 9: Green Fluorescent Nucleic Acid Stain, represents for live bacteria; PI: Propidium Iodide, represents for dead bacteria) Scale bar: 200 μm. e) Bacterial DNA and f) protein in culture supernatant by indicated treatments. Data (in b, e, and i) represent mean ± standard deviation (n = 4).

($OD_{600\,nm}$ = 0.1) was incubated with various CNs (10 μg mL^{-1}), and bacterial growth was monitored every 3 h. It is clear that our synthesized CNs inhibited the proliferation of MRSA, especially for CoMn CNs, which reduced bacterial density by ≈50% compared to the control group after 24 h incubation (Figure S9, Supporting Information). Clone formation assays also confirmed a concentration-dependent decrease in MRSA colonies (**Figure** 3a,b). Subsequently, live/dead staining also showed that CoMn CNs caused the most bacterial death, indicated by strong red fluorescence, followed by Co CNs and Mn CNs (Figure 3c,d).

In response to bacterial death, it is expected that bacterial DNA and proteins would be released into the culture supernatant. To quantify the release, the DNA and protein content were measured using a One-drop spectrophotometer (Figure 3e,f). The observed patterns of DNA and protein leakage corresponded with bacterial mortality, with CoMn CN exhibiting the highest levels of leakage, followed by Co CN and Mn CN. Consistent trends were observed across various assays, including bacterial growth inhibition, colony formation, live/dead bacterial staining, and DNA and protein leakage, all of which followed the order CoMn CN > Co CN > Mn CN. Notably, these trends aligned with the OXD-like activities of the compounds (Figure 1d). Furthermore, we investigated the potential influence of these CN's POD-like activities on anti-microbial efficacy in the presence of hydrogen peroxide (H_2O_2, 50 μM). The results indicated differential inhibition of bacterial growth (Figure S10, Supporting Information) and MRSA colony formation (Figure S11, Supporting Information) across treatments, with inhibition trends mirroring the POD-like activity of the CNs, again following the order of CoMn CN > Co CN > Mn CN (Figure 1f). Based on these findings, we proposed that the synthesized Co-based CN hold a promise for further anti-microbial applications.

2.4. Anti-Inflammation Ability of Co-Based CNs

In relation to the SOD-like activity of CoMn CN, we subsequently investigated their applications in anti-inflammatory ability. Initially, mouse lung alveolar epithelial cells (MLE-12) and mouse leukemia monocyte macrophage cells (RAW 264.7) were incubated with various CNs. These CNs demonstrated favorable cell viability at low concentrations (Figures S12 and S13, Supporting Information) and exhibited only minor cytotoxicity at higher concentrations.

Given these CNs' positive impact on cell viability, their anti-inflammatory potential was further explored, as illustrated in

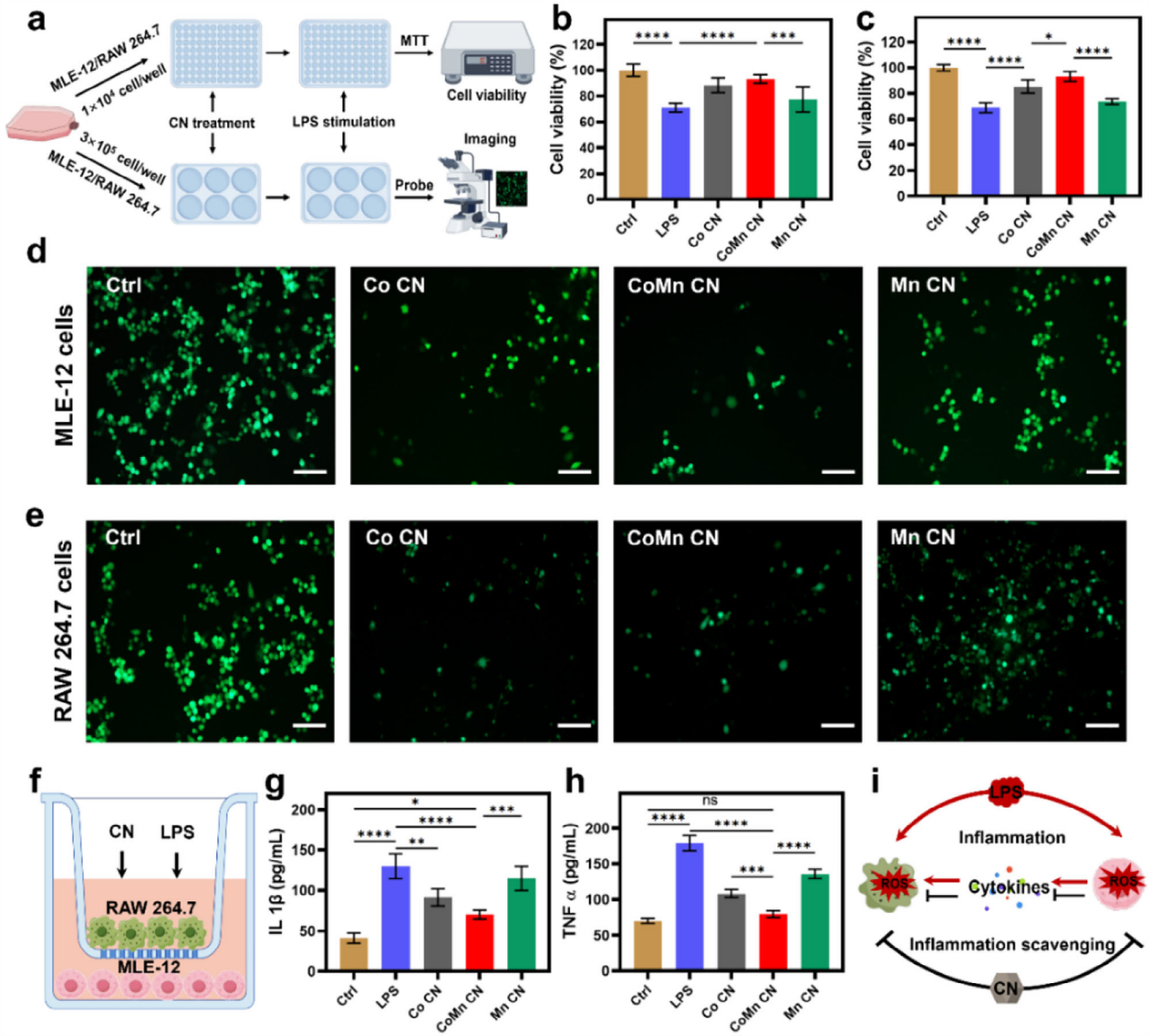

Figure 4. Anti-inflammation evaluation of Co-based CNs. a) Schematic of anti-inflammation analysis. Analysis of LPS-induced cytotoxicity for b) MLE-12 cell and c) RAW 264.7 cell with nanozyme pre-treatments. Imaging cellular ROS by using d) DCFH-DA for MLE-12 cell and e) RAW 264.7 cell by indicated treatments. f) Schematic for cytokines' detection. g) IL 1β content in culture supernatant after different treatments. f) TNF α content in culture supernatant after different treatments. i) Mechanistic description of anti-inflammation ability of Co-based CNs. Data (in b, c, g, and h) represent mean ± standard deviation (n = 4). Ordinary one-way ANOVA was used for discrepancy analysis ($^{*}p < 0.05$, $^{**}p < 0.01$, $^{***}p < 0.001$, $^{****}p < 0.0001$, ns represents not significant). Scale bar: 200 µm.

Figure 4a. Cells were pre-treated with 10 µg mL^{-1} CNs, followed by the addition of 20 µg mL^{-1} LPS. Both cell viability and ROS levels were evaluated. Our findings indicated that the designed CNs could mitigate LPS-induced cytotoxicity in both MLE-12 (Figure 4b) and RAW 264.7 cells (Figure 4c). The CoMn CN pre-treatment group exhibited the highest cell viability, followed by the Co CN and Mn CN pre-treatment groups. This variation in protective efficacy among the different treatments corresponded with the differences in their SOD-like activities (Figure 1h). The protective capacity among CNs was further corroborated through cellular ROS imaging by using 2′,7′-dichlorodihydrofluorescein diacetate (DCFH-DA, as a fluorescent probe for ROS detection). CoMn CN exhibited the most effective ROS scavenging ability in both MLE-12 (Figure 4d) and RAW 264.7 (Figure 4e) cell lines. Additionally, cytokines as the indicators of inflammatory response, were examined using a Transwell co-culture system. In this system, MLE-12 cells were cultured in the upper chamber, while RAW 264.7 cells were cultured in the lower chamber (Figure 4f). The cells were pre-treated with or without various CNs, and LPS was introduced as an inflammatory stimulus. Subsequently, cytokines such as interleukin 1β (IL 1β) and tumor necrosis factor α (TNF α) in the culture medium were quantified (Figure 4g,h). The expression levels of IL 1β and TNF α were significantly reduced in CNs-treated groups, and CoMn CN

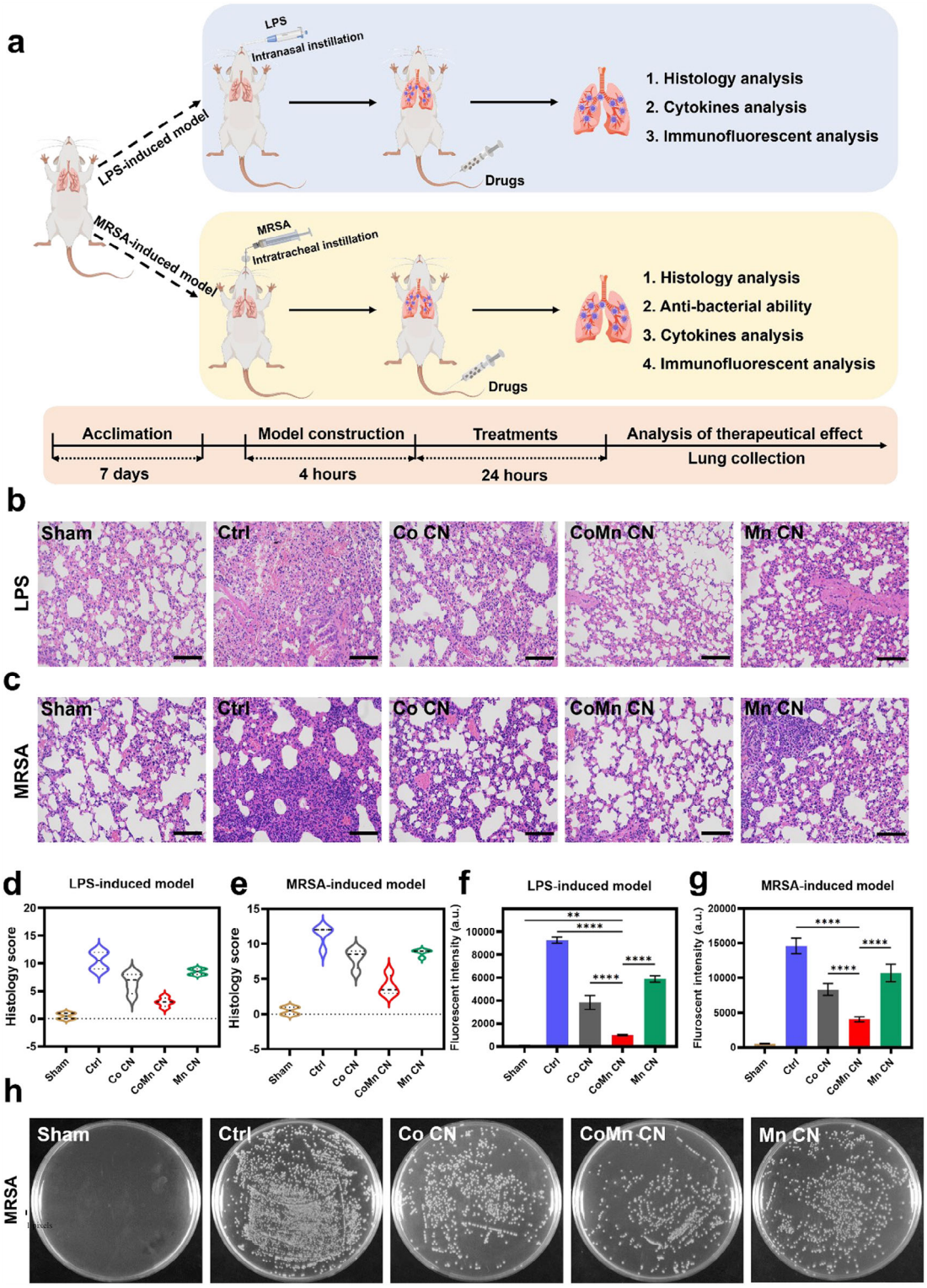

Figure 5. Co-based CNs-mediated ALI treatments. a) Schematic description of both LPS- and MRSA-induced ALI construction and treatments. b) Histopathological staining of dissected lungs by different treatments in LPS-induced ALI models. c) Histopathological staining of dissected lungs by different treatments in MRSA-induced ALI models. Histologic score of dissected lungs by different treatments in (d) LPS-induced ALI and e) MRSA-induced ALI. Quantification of ROS intensity in lung tissues by indicated treatments for f) LPS-induced ALI and g) MRSA-induced ALI. (h) Digital photos of MRSA colony formation in lung washes. Data (in d,e) are shown by violin plot (n = 4). Data (in f and g) represent mean ± standard deviation (n = 4). Ordinary one-way ANOVA was used for discrepancy analysis ($^{*}p < 0.05$, $^{**}p < 0.01$, $^{***}p < 0.001$, $^{****}p < 0.0001$, ns represents not significant). Scale bar (in b,c) is 100 µm.

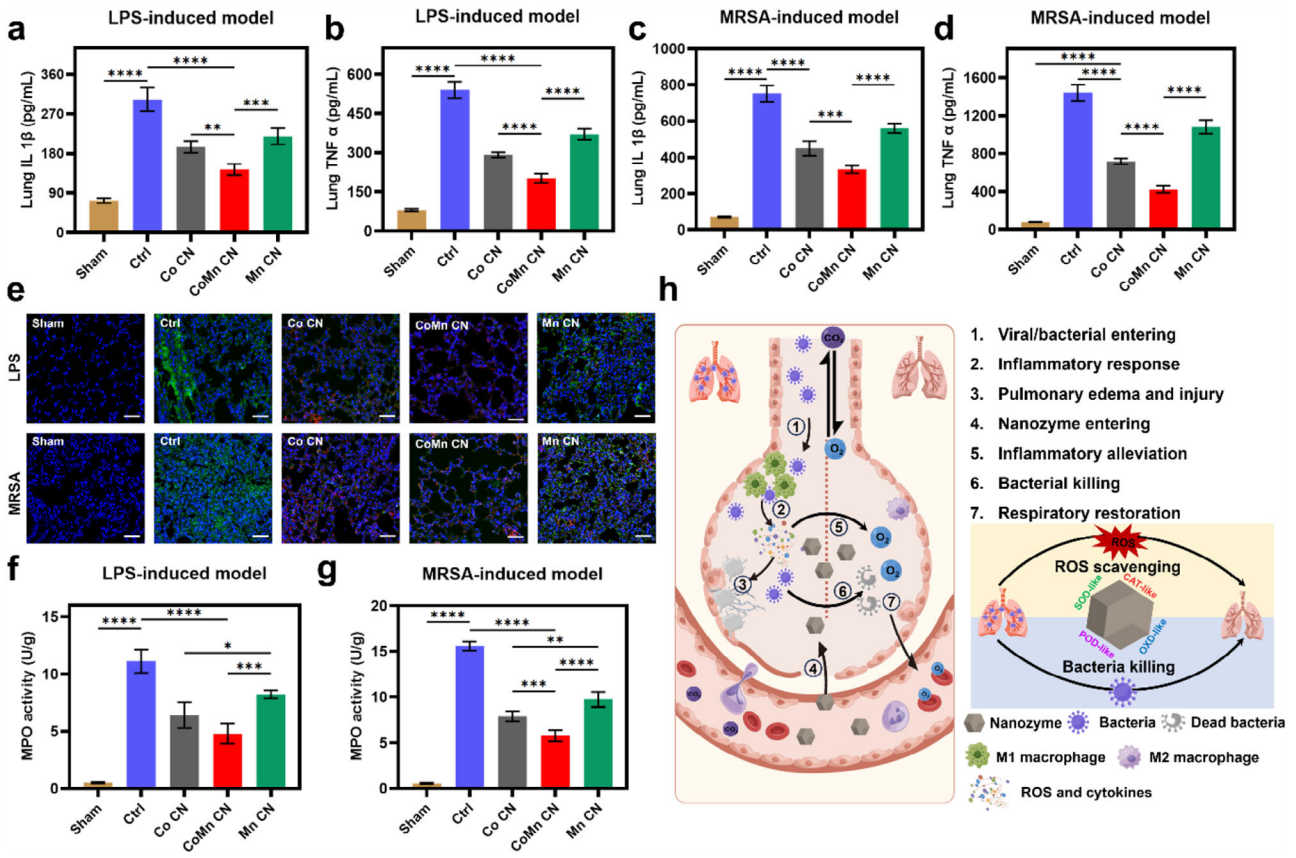

Figure 6. Evaluation of Co-based CNs-mediated inflammatory alleviation. a) IL 1β content in lung of LPS-induced ALI model. b) TNF α content in lung of LPS-induced ALI model. c) IL 1β content in lung of MRSA-induced ALI model. d) TNF α content in lung of MRSA-induced ALI model. e) Immunofluorescent images of co-staining macrophages' markers CD11c (green fluorescence, represents M1 type macrophage, indicating inflammatory response) and CD206 (red fluorescence, represents M2 type macrophage, indicating inflammatory inhibition) both for LPS and MRSA-induced ALI models. MPO content of homogenized lung in (f) LPS-induce ALI model and g) MRSA-induced ALI model. h) Scheme of Co-based CNs for ALI therapy both in inflammatory alleviation and bacteria killing. Data (in a–d and f,g) represent mean ± standard deviation (n = 4). Ordinary one-way ANOVA was used for discrepancy analysis ($^{*}p < 0.05$, $^{**}p < 0.01$, $^{***}p < 0.001$, $^{****}p < 0.0001$, ns represents not significant). Scale bar (in e) is 100 µm.

demonstrated the most effective protection by the largest down-regulating cytokine expression. Based on these findings related to ROS and inflammatory scavenging, we concluded that our synthesized Co-based CNs hold potential for facilitating inflammation scavenging (Figure 4i).

2.5. Co-Based CNs-Mediated ALI Treatment

ALI is characterized by an excessive ROS and inflammatory response. Targeting ROS and inflammatory alleviation presents a potential therapeutic strategy for ALI, as noted in previous studies.[21,23] Moreover, in models of ALI containing bacterial infection, anti-microbial capabilities are also crucial. In view of our synthesized Co-based nanozymes' performances on both anti-microbial and inflammatory scavenging, we explored these Co-based CNs for both LPS and MRSA-induced ALI treatments (**Figure 5a**). Initially, the biosafety of these CNs was assessed through intravenous administration. Histopathological analysis of major organs (Figure S14, Supporting Information) and biomarker assessments of liver and kidney function in blood serum (Figures S15 and S16, Supporting Information) revealed no significant damage, indicating a favorable safety profile for further ALI treatments. Subsequently, ALI models induced by LPS and MRSA were established. For the LPS-induced model, LPS was administered intranasally at a dose of 8 mg kg^{-1}, followed by the administration of CNs at a dose of 5 mg kg^{-1}, 4 h post-LPS treatment. All experimental mice were sacrificed for subsequent analyses at 24 h postinjection. For MRSA-induced ALI model, MRSA was instilled intratracheally at a concentration of 50 µL MRSA (1×10^{9} CFU/mL). The CNs' treatments were administered in a manner similar to that used in the LPS-induced model.

Histopathological analysis of lung tissue, as depicted in Figure 5b,c, revealed that the CoMn CN-treated group exhibited a significant protection in pulmonary edema and lung injury compared to the control group. This amelioration was further corroborated by the wet/dry lung weight ratio (Figure S17, Supporting Information) and histologic scoring (Figure 5d,e), with CoMn CN demonstrating superior protective effects against ALI, followed sequentially by Co CN and Mn CN treatments. Given that excessive ROS as a hallmark of ALI, ROS levels in lung tissues were assessed using dihydroethidium (DHE) staining (Figures S18 and S19, Supporting Information). The CoMn

CN-treated group showed a marked decrease in ROS intensity (Figure 5f,g), aligning with its observed SOD-like activity (Figure 1h). Furthermore, for MRSA-induced ALI, the bacterial load in the lungs was evaluated by colony formation, revealing that the CoMn CN-treated group had the lowest bacterial colony formation (Figure 5h) and colony forming units (Figure S20, Supporting Information), which were consistent with its anti-microbial ability (Figure 3a–d). From above, we regarded that our synthesized CoMn CN significantly alleviated ALI in vivo.

2.6. Inflammatory Alleviation for ALI by Co-Based CNs

Building upon the above-discussed CoMn CN-mediated ROS scavenging and anti-microbial properties, we conducted a systematic investigation into their anti-inflammatory potential. The expression levels of cytokines, which serve as indicators of inflammatory response,[42] were assessed by measuring the content of IL 1β and TNF α in the lung tissue of mice with ALI (**Figure 6**a–d). The group treated with CoMn CN exhibited a significant reduction in these cytokine levels. Similarly, in both LPS and MRSA-induced ALI models, the CoMn CN-treated group showed the lowest serum content of IL 1β and TNF α (Figures S21 and S22, Supporting Information), confirming the efficacy of CoMn CN in mitigating the inflammatory response. Furthermore, the infiltration of inflammatory cells was examined by co-staining for macrophage markers CD11c (green fluorescence, represents M1 type macrophage, indicating inflammatory response) and CD206 (red fluorescence, represents M2 type macrophage, indicating inflammatory inhibition). As illustrated in Figure 6e, a substantial presence of M1 macrophages was observed in both LPS and MRSA-induced ALI models. However, treatment with CoMn CN resulted in a significant increase in M2 type macrophages and a noticeable decrease in M1 type macrophages, indicating effective inhibition of inflammation in ALI. Myeloperoxidase (MPO) serves as a biomarker for oxidative stress.[43,44] In this study, MPO levels were quantified in homogenized lung tissue. Treatment with CoMn CN resulted in a significant reduction of MPO levels in both LPS and MRSA-induced models (Figure 6f,g), a finding corroborated by MPO immunohistochemical analysis (Figures S23 and S24, Supporting Information). Additionally, malondialdehyde (MDA), a crucial ROS neutralizer,[43,44] was markedly decreased following CoMn CN treatment in both models (Figure S25, Supporting Information), suggesting a reduction in inflammation. These findings, alongside cytokine detection, macrophage type analysis, and the assessment of MPO and MDA, consistently indicated an enhanced lung protection (Figure 5). In summary, our CoMn CN formulation effectively facilitates both inflammation alleviation and bacterial clearance through its diverse enzyme-like activities, as detailed in the CoMn CN-mediated acute lung injury (ALI) therapy steps illustrated in Figure 6h.

3. Conclusion

In conclusion, we developed a hetero-elemental (Mn) doping Co-based CN, CoMn CN. The co-doping Mn resulted in enhanced enzyme-like activities for the CoMn CNs comparing to the Co CNs. We attributed this enhancement to the regulation of Co's active sites, including changes of its oxidation state and the number of Co—N coordination. Given their enzymatic performance, we investigated the potential of these Co-based CNs for treating both LPS- and MRSA-induced ALIs. The CoMn CNs exhibited significant ROS and inflammatory scavenging abilities due to Mn doping, with their ROS and inflammation scavenging abilities being 1.43-fold and 1.57-fold higher than those of Co CN. The anti-microbial ability of CoMn CN was attributed to its OXD- and POD-like activities in a pH dependent manner. CoMn CN also demonstrated some bacterial killing capacity. In principle, quickly reducing inflammation and ROS is more important in the ALI animal model. We hypothesized that SOD- and CAT-like activities would first work to defend against overwhelming inflammation and ROS in ALI, while OXD- and POD-like activities could act as a second defense for bacteria scavenging. Combining these two steps, a comprehensive ALI therapeutic system was developed. This hypothesis was consistent with our results for inflammation scavenging (Figure 6) and anti-bacterial ability (Figure 5h). This study not only broadens the application of Co-based CNs but also presents a promising strategy for ALI therapy.

Supporting Information

Supporting Information is available from the Wiley Online Library or from the author.

Acknowledgements

Thanks www.home-for-researchers.com for help in writing polish and drawing schemes. Funding: This work was funded by the National Key R&D Program of China (2021YFF1200700 and 2019YFA0709200), the National Natural Science Foundation of China (22374071), Jiangsu Provincial Key R&D Program (BE2022836), the Open Funds of NMPA Key Laboratory for Biomedical Optics (20240001), State Key Laboratory of Analytical Chemistry for Life Science (5431ZZXM2501 and 5431ZZXM2306), and the Fundamental Research Funds for the Central Universities (202200325 and 021314380228).

Conflict of Interest

The authors declare no conflict of interest.

Data Availability Statement

The data that support the findings of this study are available from the corresponding author upon reasonable request.

Keywords

acute lung injury, enzyme mimics, hetero-element-doped carbon nanozymes, nanocatalytic therapy, pneumonia

Received: February 8, 2025
Revised: May 12, 2025
Published online:

[1] A. Torres, C. Cilloniz, M. S. Niederman, R. Menéndez, J. D. Chalmers, R. G. Wunderink, T. P van der Poll, *Nat. Rev. Dis. Primers* **2021**, *7*, 25.
[2] M. E. Long, R. K. Mallampalli, J. C. Horowitz, *Clin. Sci.* **2022**, *136*, 747.
[3] S. Jain, W. H. Self, R. G. Wunderink, S. Fakhran, R. Balk, A. M. Bramley, C. Reed, C. G. Grijalva, E. J. Anderson, D. M. Courtney, J. D. Chappell, C. Qi, E. M. Hart, F. Carroll, C. Trabue, H. K. Donnelly, D. J. Williams, Y. Zhu, S. R. Arnold, K. Ampofo, G. W. Waterer, M. Levine, S. Lindstrom, J. M. Winchell, J. M. Katz, D. Erdman, E. Schneider, L. A. Hicks, J. A. McCullers, A. T. Pavia, et al., *N. Engl. J. Med.* **2015**, *373*, 415.
[4] M. R. Hendricks, L. P. Lashua, D. K. Fischer, B. A. Flitter, K. M. Eichinger, J. E. Durbin, S. N. Sarkar, C. B. Coyne, K. M. Empey, J. M. Bomberger, *Proc. Natl. Acad. Sci* **2016**, *113*, 1642
[5] I. S. Kamat, V. Ramachandran, H. Eswaran, D. Guffey, D. M. Musher, *Clin. Infect. Dis.* **2020**, *70*, 538.
[6] A. Nadeem, N. Al-Harbi, S. Ahmad, K. Ibrahim, N. Siddiqui, M. Al-Harbi, *Clin. Exp. Immunol.* **2018**, *191*, 279.
[7] G.-w. Tu, Y. Shi, Y.-j. Zheng, M.-j. Ju, H.-y. He, G.-g. Ma, G.-w. Hao, Z. Luo, *J. Transl. Med.* **2017**, *15*, 181.
[8] F. M. de Benedictis, E. Kerem, A. B. Chang, A. A. Colin, H. J. Zar, A. Bush, *Lancet* **2020**, *396*, 786.
[9] Y. Jiang, Y. Deng, H. Pang, T. Ma, Q. Ye, Q. Chen, H. Chen, Z. Hu, C.-F. Qin, Z. Xu, *Cell Discov.* **2022**, *8*, 38.
[10] A. Aslan, C. Aslan, N. M. Zolbaning, R. Jafari, *Pneumonia* **2021**, *13*, 14.
[11] G. F. Nieman, L. A. Gatto, P. Andrews, J. Satalin, L. Camporota, B. Daxon, S. J. Blair, H. Al-khalisy, M. Madden, M. Kollisch-Singule, H. Aiash, N. M. Habashi, *Ann. Intensive Care* **2020**, *10*, 3.
[12] X. Fu, X. Yu, J. Jiang, J. Yang, L. Chen, Z. Yang, C. Yu, *Nat. Commun.* **2022**, *13*, 6528.
[13] Y. Song, Q. You, X. Chen, *Adv. Mater.* **2023**, *35*, 2212102.
[14] T. Liu, B. Xiao, F. Xiang, J. Tan, Z. Chen, X. Zhang, C. Wu, Z. Mao, G. Luo, X. Chen, J. Deng, *Nat. Commun.* **2020**, *11*, 2788.
[15] D. Jiang, D. Ni, Z. T. Rosenkrans, P. Huang, X. Yan, W. Cai, *Chem. Soc. Rev.* **2019**, *48*, 3683.
[16] H. S. Kim, S. Lee, D. Y. Lee, *Small* **2023**, *19*, 2302331.
[17] D. K. Min, Y. E. Kim, M. K. Kim, S. W. Choi, N. Park, J. Kim, *ACS Nano* **2023**, *17*, 24404.
[18] Y. Feng, F. Chen, J. M. Rosenholm, L. Liu, H. Zhang, *Mater. Futures* **2022**, *1*, 023502.
[19] A. S. Pugazhendhi, C. J. Neal, K. M. Ta, M. Molinari, U. Kumar, F. Wei, E. Kolanthai, A. Ady, C. Drake, M. Hughes, S. Yooseph, S. Seal, M. J. Coathup, *Biomaterials* **2024**, *307*, 122527.
[20] H. Ji, C. Zhang, F. Xu, Q. Mao, R. Xia, M. Chen, W. Wang, S. Lv, W. Li, X. Shi, *Adv. Sci.* **2022**, *9*, 2201696.
[21] L. Yue, C. Gao, J. Li, H. Chen, S. M. Y. Lee, R. Luo, R. Wang, *Adv. Mater.* **2023**, *35*, 2211626.
[22] X. Wu, B. Wang, Y. Li, X. Guan, M. Yin, W. Lv, Y. Chen, F. Lu, T. Qin, H. Gao, W. Jin, Y. Huang, C. Li, M. Gao, J. Lu, *Chin. Chem. Lett.* **2024**, *36*, 110211.
[23] R. Yuan, Y. Li, S. Han, X. Chen, J. Chen, J. He, H. Gao, Y. Yang, S. Yang, Y. Yang, *ACS Cent. Sci.* **2022**, *8*, 10.
[24] J. Li, X. Cai, P. Jiang, H. Wang, S. Zhang, T. Sun, C. Chen, K. Fan, *Adv. Mater.* **2024**, *36*, 2307337.
[25] M. Lu, B. Li, L. Guan, K. Li, Y. Lin, *ACS Sustainable Chem. Eng.* **2019**, *7*, 15471.
[26] F. Duan, Q. Jia, G. Liang, M. Wang, L. Zhu, K. J. McHugh, L. Jing, M. Du, Z. Zhang, *ACS Nano* **2023**, *17*, 12140.
[27] X. Zhang, A. Yuan, X. Mao, Q. Chen, Y. Huang, *Sensor. Actuat. B: Chem.* **2019**, *299*, 126928.
[28] S. He, J. Huang, Q. Zhang, W. Zhao, Z. Xu, W. Zhang, *Adv. Funct. Mater.* **2021**, *31*, 2105198.
[29] K. Xu, M. Chang, Z. Wang, H. Yang, Y. Jia, W. Xu, B. Zhao, Y. Chen, F. Yao, *Adv. Mater.* **2023**, *35*, 2302961.
[30] Q. Chen, X. Zhang, S. Li, J. Tan, C. Xu, Y. Huang, *Chem. Eng. J.* **2020**, *395*, 125130.
[31] S.-N. Song, X.-L. Zhao, X.-C. Yang, Y. Ding, F.-D. Ren, X.-Y. Pang, B. Li, J.-Y. Hu, Y.-Z. Chen, W.-W. Gao, *ACS Appl. Mater. Interfaces* **2024**, *16*, 16011.
[32] J. Wang, Y. Wang, D. Zhang, C. Chen, *ACS Appl. Mater. Interfaces* **2020**, *12*, 29614.
[33] Y. Yang, Z. Li, X. Fan, C. Jiang, J. Wang, Y. Rastegar-Kashkooli, T. J. Wang, J. Wang, M. Wang, N. Cheng, X. Yuan, X. Chen, B. Jiang, J. Wang, *ACS Nano* **2024**, *18*, 16450.
[34] Y. Cheng, C. Cheng, J. Yao, Y. Yu, Y. Liu, H. Zhang, L. Miao, H. Wei, *Adv. Therap.* **2021**, *4*, 2100081.
[35] J. Yao, Y. Cheng, M. Zhou, S. Zhao, S. Lin, X. Wang, J. Wu, S. Li, H. Wei, *Chem. Sci.* **2018**, *9*, 2927.
[36] Z. Li, F. Liu, C. Chen, Y. Jiang, P. Ni, N. Song, Y. Hu, S. Xi, M. Liang, Y. Lu, *Nano Lett.* **2023**, *23*, 1505.
[37] P. Yu, L. Wang, F. Sun, Y. Xie, X. Liu, J. Ma, X. Wang, C. Tian, J. Li, H. Fu, *Adv. Mater.* **2019**, *31*, 1901666.
[38] H. Li, G. Yan, H. Zhao, P. C. Howlett, X. Wang, J. Fang, *Adv. Mater.* **2024**, *36*, 2311272.
[39] X. Chen, Y. Feng, H. Wang, Y. Jiang, Z. Zhai, H. Li, *Mater. Chem. Phys.* **2022**, *289*, 126514.
[40] Y. He, Q. Tan, L. Lu, J. Sokolowski, G. Wu, *Electrochem. Energy Rev.* **2019**, *2*, 231.
[41] G. Belardi, R. Lavecchia, F. Medici, L. Piga, *Waste Manage.* **2012**, *32*, 1945.
[42] Q. Ma, Q. Fan, J. Xu, J. Bai, X. Han, Z. Dong, X. Zhou, Z. Liu, Z. Gu, C. Wang, *Matter* **2020**, *3*, 287.
[43] J. Yang, S. Duan, H. Ye, C. Ge, C. Piao, Y. Chen, M. Lee, L. Yin, *Adv. Funct. Mater.* **2021**, *31*, 2008960.
[44] Z. Li, Y. Feng, S. Zhang, T. Li, H. Li, D. Wang, K. Hao, C. He, H. Tian, X. Chen, *ACS Nano* **2023**, *17*, 8551.